The Journal of Chemical Physics

RESEARCH ARTICLE | JANUARY 10 2023

Modular mixing in plasmonic metal oxide nanocrystal gels with thermoreversible links

Jiho Kang; Zachary M. Sherman; Hannah S. N. Crory; ... et. al

J. Chem. Phys. 158, 024903 (2023)
https://doi.org/10.1063/5.0130817

AIP Publishing

The Journal of Chemical Physics ARTICLE scitation.org/journal/jcp

Modular mixing in plasmonic metal oxide nanocrystal gels with thermoreversible links

Cite as: J. Chem. Phys. 158, 024903 (2023); doi: 10.1063/5.0130817
Submitted: 14 October 2022 • Accepted: 22 December 2022 •
Published Online: 10 January 2023

Jiho Kang,[1] Zachary M. Sherman,[1] Hannah S. N. Crory,[2] Diana L. Conrad,[2] Marina W. Berry,[2] Benjamin J. Roman,[1] Eric V. Anslyn,[2,a)] Thomas M. Truskett,[1,3,b)] and Delia J. Milliron[1,2,c)]

AFFILIATIONS

[1] McKetta Department of Chemical Engineering, University of Texas at Austin, Austin, Texas 78712, USA
[2] Department of Chemistry, University of Texas at Austin, Austin, Texas 78712, USA
[3] Department of Physics, University of Texas at Austin, Austin, Texas 78712, USA

Note: This paper is part of the JCP Special Topic on Colloidal Gels.
[a)] **Electronic mail:** anslyn@austin.utexas.edu
[b)] **Electronic mail:** truskett@che.utexas.edu
[c)] **Author to whom correspondence should be addressed:** milliron@che.utexas.edu

ABSTRACT

Gelation offers a powerful strategy to assemble plasmonic nanocrystal networks incorporating both the distinctive optical properties of constituent building blocks and customizable collective properties. Beyond what a single-component assembly can offer, the characteristics of nanocrystal networks can be tuned in a broader range when two or more components are intimately combined. Here, we demonstrate mixed nanocrystal gel networks using thermoresponsive metal–terpyridine links that enable rapid gel assembly and disassembly with thermal cycling. Plasmonic indium oxide nanocrystals with different sizes, doping concentrations, and shapes are reliably intermixed in linked gel assemblies, exhibiting collective infrared absorption that reflects the contributions of each component while also deviating systematically from a linear combination of the spectra for single-component gels. We extend a many-bodied, mutual polarization method to simulate the optical response of mixed nanocrystal gels, reproducing the experimental trends with no free parameters and revealing that spectral deviations originate from cross-coupling between nanocrystals with distinct plasmonic properties. Our thermoreversible linking strategy directs the assembly of mixed nanocrystal gels with continuously tunable far- and near-field optical properties that are distinct from those of the building blocks or mixed close-packed structures.

I. INTRODUCTION

Colloidal nanocrystals, inorganic nanoparticles commonly stabilized by organic capping ligands, have distinctive optical responses, including localized surface plasmon resonance (LSPR).[1–5] When organized into assemblies, nanocrystals display emergent structure-dependent properties. For example, stimuli-responsive hydrogels with embedded nanocrystals can exhibit a diverse array of switchable properties, including surface enhanced Raman scattering,[6] plasmonic circular dichroism,[7] optical birefringence,[8] and circularly polarized luminescence.[9]

Nanocrystal gels, whose colloidal building blocks organize into low-density, percolating networks, are increasingly recognized as promising candidates for functional materials. Their advantages, relative to close-packed assemblies, include simple fabrication, structural tunability, and the potential for rapid reversibility.[10–13] Gels can, however, be challenging to control and characterize, having heterogeneous structures across length scales, and their properties can be challenging to simulate since large systems are required to effectively capture that complexity. Different gelation methods, such as controlled destabilization, direct bridging, depletion, and linking with secondary molecules, have been developed to rationally control nanocrystal interactions and the resulting gel structures.[14]

Although the design and synthesis of colloidal nanocrystals with microscopically limited valence, e.g., due to a precise number of surface binding sites, is often impractical,[15,16] macroscopically (i.e., statistically) controlled valence can be achieved in linker-mediated assembly by choosing the ratio of molecular linkers to colloids in

the system.[13,17–32] Linker directed assembly is a modular strategy that can be applied to building blocks of different sizes, shapes, and elemental compositions, although the collective properties of the assemblies can also be influenced by the characteristics of the linking molecules[20,26,31] or the linker bonds.[28,29,33,34]

The co-assembly of multiple nanocrystal components broadens the range of properties attainable in assemblies. Even mixing nanoparticles with distinct optical properties in dispersions allows targeting of optical properties such as specific spectral transparency windows,[35] although emergent properties based on nanoparticle interactions are lacking in such systems. Close-packed binary nanoparticle superlattices with various superatomic structures have been assembled from noble metals, semiconductors, oxides, and magnetic alloys;[36–38] examples with intermixed CdSe quantum dots and Au nanoparticles showed photoluminescence quenching via Forster resonance energy transfer.[39,40] However, small differences in nanocrystal size and shape can lead to non-uniform intermixing,[36,41,42] making it challenging to reliably tune the properties of multi-component superlattices. On the other hand, nanocrystal gels, which lack long-range order, largely avoid such restrictions on compatibility, allowing a more flexible combination of disparate components.[43–52] As an illustrative example, Davis *et al.* demonstrated that the extent of intermixing of two-component (ZnS and CdSe) aerogels can be kinetically controlled by judicious selection of capping ligands on the nanocrystals.[49]

In molecularly linked mixed gels of Au nanoparticles and CdTe nanocrystal quantum dots, photoluminescence quenching could be continuously tuned by varying the compositional mixing ratio.[43] Similarly, co-gelation of Au nanoparticles and luminescent CdSe/CdS core/shell nanorods produced homogeneous nanoparticle networks where the spatial extent of fluorescence quenching could be systematically modulated by changing the ratio of Au nanoparticles to nanorods, showing marked differences compared to the properties of mixed colloidal dispersions.[50] Wolf *et al.* prepared a white-light emitting aerogel by co-gelation of UV-blue-emitting ZnSe with red- and yellow-emitting CdTe quantum dots.[44] More recently, CdSe/CdS dot/rod nanocrystal-based aerogels were prepared with varying proportions of building blocks with differently sized CdSe cores, and hence distinct emission colors, highlighting how mixing can be used to color-tune the resulting nanocrystal gel networks.[51] Several other homogeneously mixed multicomponent nanocrystal aerogels and cryoaerogels have also been reported with composition-dependent variation of optical properties.[45,48,52]

Recently, we have demonstrated infrared optical modulation by the reversible gelation of plasmonic tin-doped indium oxide (ITO) nanocrystals using a chemically and thermally responsive metal coordination linkage.[29] The rapid, reversible bonding of the links enabled highly reproducible gelation during thermal cycling and, thus, consistent—though strikingly distinct—infrared extinction spectra in the colloidal dispersion and gel states. Linking was accomplished by cobalt ions bonding with terpyridine functional groups tethered to the nanocrystals by a solubilizing polyethylene oxide-like backbone, a strategy that does not rely on specific characteristics of the nanocrystals themselves, so long as they can be similarly functionalized. As such, this versatile molecular linking approach could be applicable beyond single-component assemblies, offering ready access to tunable, switchable optical properties by simply mixing components without reengineering the constituent nanocrystals or the chemistry used for assembly.

Here, we demonstrate fully thermoreversible, multi-component gel assemblies comprising mixtures of plasmonic ITO nanocrystals. ITO nanocrystals are excellent building blocks to study emergent optical properties of assemblies because synthetic methods allow precise tuning of their size, shape, and plasmonic extinction spectra, where the resonant frequency is continuously tunable across the mid- and near-infrared by variation of the tin doping concentration. Using small angle X-ray scattering (SAXS) and electron microscopy, we show that ITO nanocrystals with different sizes, dopant concentrations, and shapes can be incorporated at arbitrary ratios in randomly mixed gel networks. Extinction spectral lineshapes can be approximated by weighted averages of the spectra of single-component assemblies, yet systematic deviations arise when varying mixing ratios of nanocrystal building blocks with different resonant frequencies. As such, we find the plasmonic spectra reflect cross-coupling effects that change both the frequency and intensity of the contributions from each component depending on the relative sizes and the mixing ratio of the nanocrystals. Using Brownian dynamics (BD) simulations and a recently introduced mutual polarization method (MPM) for computing the optical response of structurally complex assemblies,[53] we show that mixing counterintuitively *sharpens* the far-field spectral components of the gels, while simultaneously broadening the distribution of near-field hotspot intensities. The modular nature of the gel assembly process suggests wide-ranging compositions of nanoparticles could be combined in mixed gels, while different linker chemistries and characteristics could be used to vary gel structure. The opportunities are vast to mix and match components in this scheme to customize optical absorption, emission, and more.

II. METHODS

A. Experiments

1. Synthesis and ligand functionalization of nanocrystals

ITO nanocrystals were synthesized on a Schlenk line via a modified slow injection procedure.[23,29,54] Briefly, a mixture of Sn(IV)acetate (142.0 mg, 0.4 mmol for 4 at. % Sn nanocrystals or 283.9 mg, 0.8 mmol for 8 at. % Sn nanocrystals) and In(III)acetate (2.803 g, 9.6 mmol for 4 at. % Sn nanocrystals or 2.686 g, 9.2 mmol for 8 at. % Sn nanocrystals) was dissolved in 20 ml of oleic acid, degassed under vacuum for an hour at 90 °C, and put under flowing nitrogen for 3 h with stirring at 150 °C. The precursor solution was injected dropwise into 13 ml of oleyl alcohol maintained at 290 °C under flowing nitrogen. The injection volume was adjusted to control the size of the nanocrystals. Finally, the nanocrystals were washed five times with ethanol and dispersed in hexane. Exact Sn doping concentrations were determined by inductively coupled plasma optical emission spectroscopy (ICP-OES) analysis.

Fluorine-, tin-co-doped indium oxide (FITO) nanocubes were similarly synthesized on a Schlenk line by modification of previously reported protocols.[55,56] Briefly, In(III)acetate (1.343 g, 4.6 mmol), Sn(IV)fluoride (48.68 mg, 0.25 mmol), Sn(IV)acetate (70.96 mg, 0.2 mmol), and 10 ml of oleic acid were mixed in a three-neck round-bottom flask in a nitrogen-filled glovebox, transferred to a Schlenk

line, and degassed under vacuum at 120 °C for 15 min. The precursor solution was injected dropwise into 13 ml of oleyl alcohol maintained at 290 °C and vented with a 19-gauge needle under nitrogen gas flow. The nanocrystals were washed three times with ethanol and dispersed in hexane.

Terpyridine-functional ligands (**TLs**) were synthesized in the manner previously published.[29] Briefly, solid-phase peptide synthesis (SPPS) was performed, producing a resin-bound peptide strand incorporating azidolysine. The terpyridine functionality was added to the terminal azide via solid-phase copper azide alkyne cycloaddition (SP-CuAAC), producing the resin-bound terpyridine-functionalized ligand strand. Finally, the ligand was cleaved from the resin, followed by purification by high performance liquid chromatography and lyophilization prior to use.

To prepare **TL**-functionalized ITO nanospheres (**TL**-ITO), a precipitated, dried pellet of as-synthesized ITO nanocrystals (oleate-ITO) was sonicated in ligand solution [0.01M **TL** in *N*,*N*-dimethylformamide (DMF)] for 1 h, washed two times with a 2:3 solution of ethanol:hexane, and finally dispersed in DMF. **TL**-functionalized FITO nano cubes (**TL**-FITO) were prepared by stirring a dried pellet of as-synthesized FITO nanocrystals (oleate-FITO) in ligand solution (0.01M **TL** in DMF) for two days, washing one time with a 2:3 solution of ethanol:hexane, and finally dispersing in DMF.

2. Preparation of mixed nanocrystal gel assemblies

To prepare the samples, Co^{2+} (0.01M anhydrous $CoCl_2$, in DMF) and Cl^- (0.5M tetrabutylammonium chloride, or TBACl, in DMF) were added to a two-component dispersion of **TL**-functionalized nanocrystals (40.0 mg/ml, in DMF) mixed beforehand at a desired ratio. The final volume fraction of nanocrystals was diluted to 0.001 by adding DMF. The final concentrations of $CoCl_2$ and TBACl were 0.5 and 150 mM, respectively.

3. Small-angle X-ray scattering (SAXS)

Transmission SAXS was performed on the SAXSLAB Ganesha at the University of Texas at Austin, Texas Materials Institute. Nanocrystal dispersions and gels were contained in thin-walled glass capillaries (Charles Supper Company, Inc.) and flame-sealed before measurement. A silver behenate standard was used to calibrate the sample-to-detector distance (~1 m). SAXS data were analyzed using the Irena and Nika software packages in Igor Pro 8.

4. UV–vis–NIR spectroscopy

All LSPR absorption spectra were collected on an Agilent-Cary 5000 spectrophotometer. The absorption spectra of oleate-ITO dispersed in tetrachloroethylene were collected using a quartz cuvette with a 2 mm pathlength (Spectrocell, Inc.). To obtain gel absorption spectra, mixed nanocrystal gels were first turned into a free-flowing dispersion on a hotplate at 120 °C, injected into a liquid cell comprising two 2-mm-thick CaF_2 windows separated by a 56-μm-thick spacer (Harrick Scientific Products, Inc.), and finally cooled to room temperature for measurement.

5. Deconvolution of the infrared response of mixed gels

The experimental infrared responses of mixed gels were deconvoluted into high- and low-frequency spectral contributions using exponentially modified Gaussian distribution fits. First, the spectra of single-component gels were fitted to determine μ, σ, λ, and C,

$$f_1(x) = Cf(x) = \frac{1}{2}C\lambda e^{\lambda(2\mu+\lambda\sigma^2-2x)/2}\,\mathrm{erfc}\left(\frac{\mu+\lambda\sigma^2-x}{\sqrt{2}\sigma}\right). \quad (1)$$

Next, the spectra of mixed gels comprising nanocrystals of types i and j were fitted,

$$f_2(x) = \eta_i C_{1,i} f(x;\mu_i,\lambda_{1,i},\sigma_i) + (1-\eta_i)C_{1,j} f(x;\mu_j,\lambda_{1,j},\sigma_j), \quad (2)$$

where $C_{1,i}$, $\lambda_{1,i}$, $C_{1,j}$, and $\lambda_{1,j}$ are parameters determined from $f_1(x)$ fits to single-component gels comprising nanocrystals of types i and j, and η_i is the mixing fraction of nanocrystals of type i. Only the parameters μ and σ that determine the peak frequency and width of each component were allowed to vary.

B. Simulations

1. Brownian dynamics simulations of nanocrystal gels

We performed BD simulations of $N = 8000$ nanocrystals in a cubic periodic box at a volume fraction $\eta = 0.01$ using HOOMD-Blue (v2.9.7).[57] As recently demonstrated[53] and further established below, interactions between ligand-capped nanocrystals mediated by molecular links can be modeled as hard-sphere repulsion and a strong short-range effective attraction. Here, we adopt an attractive well with the same functional form as the depletion interaction,[58] but other computationally convenient forms would yield similar results.[59,60] As observed experimentally by measurements of the second virial coefficient,[61] the thermodynamic hard-sphere radii of the ligand-capped colloids, b_i, are larger than their inorganic core radii, a_i (Table S1). Specifically, the nanocrystals interacted via hard sphere repulsion for $r < b_i + b_j$,

$$U_{ij}^{\mathrm{HS}}(r) = \frac{\gamma_i^H \gamma_j^H}{2\Delta t\left(\gamma_i^H + \gamma_j^H\right)}\left(r - (b_i + b_j)\right)^2, \quad (3)$$

and the following short-ranged attraction for $b_i + b_j \le r \le b_i + b_j + 2\delta$:

$$U_{ij}^{\mathrm{attr}}(r) = -\frac{\varepsilon_{\mathrm{attr}}}{16\delta^3\left(1+\frac{3b}{2\delta}\right)r}\left(b_i + b_j + 2\delta - r\right)^2 \times \left(r^2 + 2r(b_i + b_j + 2\delta) - 3(b_i - b_j)^2\right). \quad (4)$$

Here, b is the smallest nanocrystal radius, $\gamma_i^H = 6\pi\mu b_i$ is the Stokes–Einstein hydrodynamic drag coefficient of particle i in a fluid of viscosity μ, $\Delta t = 10^{-4}\tau_D$ is the integration time step, $\tau_D = \gamma^H b^2/k_B T$ is the diffusion time of the smallest nanocrystal, $\varepsilon_{\mathrm{attr}} = 10k_B T$ is the strength of the attraction between two small nanocrystals at contact $r = 2b$, and $\delta = 0.1b$ is the range of the attractive potential. Note that this form of hard-sphere repulsion separates two overlapping particles to contact over a single time step and is, therefore, functionally equivalent to the Heyes–Melrose algorithm for hard spheres.[62] Particles were initialized on a simple cubic lattice and allowed to equilibrate with only hard sphere repulsions for $500\tau_D$. The attractions were then turned on, the suspension evolved for $10\,000\tau_D$, and assembled configurations were sampled over $1000\tau_D$.

The three-dimensional partial structure factors $S_{ij}(\mathbf{q})$ were computed on a grid of wavevectors $\mathbf{q} = (2\pi/L)[\kappa_x, \kappa_y, \kappa_z]$, where $\kappa_i = -M/2, \ldots, (M-1)/2$ and L is the box dimension, by dividing the simulation box into M^3 cubic cells with centers $\mathbf{r} = L[n_x, n_y, n_z]$, where $n_i = -M/2, \ldots, (M-1)/2$. Selecting $M = 512$, we counted the number of particles of type i in each cell $\rho_i(\mathbf{r})$, used a fast Fourier transform to estimate $\hat{\rho}_i(\mathbf{q})$, then computed $S_{ij}(\mathbf{q}) = \hat{\rho}_i\hat{\rho}_j^*/\sqrt{N_i N_j}$. We then calculated $S_{ij}(q)$ by constructing a 1D grid of bins centered at $q = 2\pi\kappa_i/L$, where $\kappa_i = 0, 1, 2, \ldots$, and averaging all $S_{ij}(\mathbf{q})$ values in the same bin. The total scattering intensity was then computed from the partial structure factors $I = x_1 f_1^2 S_{11} + 2 f_1 f_2 \sqrt{x_1 x_2} S_{12} + x_2 f_2^2 S_{22}$, where x_i is the mole fraction of i and $f_i = 4\pi a_i^3 j_1(qa_i)/(qa_i)$ is the form factor of i in terms of the spherical Bessel function j_1. The effective structure factor is then $S_{\text{eff}} = I/(x_1 f_1^2 + x_2 f_2^2)$ and is averaged over 20 configurations. The effective structure factor without intermixing of nanocrystals was estimated as $S_{\text{eff,lin}} = (x_1 f_1^2 S_{11} + x_2 f_2^2 S_{22})/(x_1 f_1^2 + x_2 f_2^2)$.

The thermodynamic hard sphere sizes were found by comparing the simulated and experimental structure factors of single-component gels and selecting the b_i that aligned the positions of the primary peak in $S(q)$ (Table S1). This procedure assigns a dimensional length scale to the nondimensional simulations. These b_i values were then held fixed in simulations of mixed nanocrystal gels.

2. Optical simulations using the mutual polarization method

The dielectric function of the nanocrystals $\varepsilon_p(\omega)$ was estimated by a core–shell Drude model,

$$\varepsilon_p = \varepsilon_s \frac{\varepsilon_c + \varepsilon_s + 2\eta_c(\varepsilon_c - \varepsilon_s)}{\varepsilon_c + 2\varepsilon_s - \eta_c(\varepsilon_c - \varepsilon_s)}, \quad \varepsilon_c = \varepsilon_\infty - \frac{\varepsilon_0 \omega_p}{\omega^2 + i\gamma\omega}, \quad \varepsilon_s = \varepsilon_\infty, \quad (5)$$

where ε_s and ε_c are the dielectric functions of the depleted shell and the core, respectively, ω is the frequency, ε_0 is the vacuum permittivity, and ε_∞ is the high-frequency permittivity. For each of the four types of nanocrystals, the plasma frequency ω_p, the damping coefficient γ, and the electron-accessible volume fraction η_c were determined by fitting the extinction spectra of dilute dispersions using the procedure described in Ref. 63. The fit parameters are shown in Table S2.

The optical response of the assembled nanocrystals when irradiated by light with electric field polarization $\mathbf{E}_0$ was computed using MPM,[53] which determines the many-bodied induced dipoles $\mathbf{p}_i$ of each nanocrystal i by solving the system of equations,

$$\mathbf{E}_0 = \sum_j \mathbf{M}_{ij} \cdot \mathbf{p}_j, \qquad \mathbf{M}_{ij} = \begin{cases} \dfrac{1}{4\pi a_i^3 \varepsilon_m \alpha_i}\mathbf{I}, & i = j, \\ \dfrac{1}{4\pi\varepsilon_m r^3}(\mathbf{I} - 3\hat{\mathbf{r}}\hat{\mathbf{r}}), & i \neq j, \end{cases} \quad (6)$$

where a_i is the core radius of i (from Table I), $\alpha_i = (\varepsilon_i - \varepsilon_m)/(\varepsilon_i + 2\varepsilon_m)$, $\varepsilon_i(\omega)$ is the permittivity of i, ε_m is the permittivity of the background fluid medium assumed real and constant over the frequencies of interest, $\mathbf{r} = \mathbf{x}_i - \mathbf{x}_j$, $r = |\mathbf{r}|$, $\hat{\mathbf{r}} = \mathbf{r}/r$, $\mathbf{x}_i$ is the position of i, and $\mathbf{I}$ is the identity tensor. The j sum in (6) runs over all nanocrystals and their periodic images and details of solving (6) are in the supplementary material. The extinction cross section of each nanocrystal is then computed,

$$\sigma_i = \frac{\sqrt{\mu_m}\omega}{\sqrt{\varepsilon_m}E_0^2} \operatorname{Im}\left[\mathbf{p}_i \cdot \mathbf{E}_0\right], \quad (7)$$

where μ_m is the permeability of the background medium, and the effective extinction cross section of the entire sample per volume of nanocrystal is $\sigma = \frac{\sum_i \sigma_i}{\sum_i 4\pi a_i^3/3}$. The absorbance was then calculated as $\eta\sigma\ell/\ln(10)$, where the total nanocrystal core volume fraction $\eta = 0.001$ and path length $\ell = 56\ \mu$m are the same as those used for UV–vis–NIR spectroscopy.

The local electric field throughout the sample is

$$\mathbf{E}(\mathbf{x}) = \mathbf{E}_0 + \sum_i \frac{1}{4\pi\varepsilon_m r^3}(3\hat{\mathbf{r}}\hat{\mathbf{r}} - \mathbf{I}) \cdot \mathbf{p}_i, \quad (8)$$

where now $\mathbf{r} = \mathbf{x} - \mathbf{x}_i$ and the i sum runs over all nanocrystals and their periodic images. We compute the local field maxima $E^2 = |\mathbf{E}|^2$ (i.e., hotspot intensities) on the surface of each nanocrystal, assumed to occur at locations $\mathbf{x}_i \pm a_i\hat{\mathbf{p}}_i''$, where $\mathbf{p}'' = \operatorname{Im}\mathbf{p}$ and $\hat{\mathbf{p}}'' = \mathbf{p}''/|\mathbf{p}''|$. Both σ and the distribution of hot-spots are averaged over 20 configurations and three independent field polarizations $\mathbf{E}_0 = E_0\hat{\mathbf{e}}_i$, $i = x, y, z$.

TABLE I. Material characterization of ITO nanocrystals.

	Sn doping (at. %)	Diameter ± std. dev. (nm)	LSPR peak position (cm^{-1})	FWHM (cm^{-1})
Sn_4-d_{11}	4.1	11.1 ± 0.9	4274	1079
Sn_8-d_{11}	7.8	11.3 ± 1.3	5297	1591
Sn_4-d_{16}	4.0	16.3 ± 1.5	4481	1308
Sn_8-d_{16}	7.9	15.8 ± 1.6	5384	1519

III. RESULTS AND DISCUSSION

A. Nanocrystal synthesis, ligand exchange, and gelation

To prepare building blocks with different optical responses and sizes for mixed-gel assemblies, ITO nanocrystals with two tin doping concentrations and two diameters were synthesized via a modified slow injection method[54] and functionalized with **TL** to facilitate gel formation via metal coordination linkages.[29] Four different ITO nanocrystals with either low or high tin doping concentration (4 or 8 at. %, respectively) and either small or large diameter (11 or 16 nm, respectively) were prepared and denoted by Sn_x-d_y to indicate ITO nanocrystals with x at. % tin doping and y nm diameter (Table I).

Bright-field scanning transmission electron microscopy (STEM) images show monodisperse, quasi-spherical nanocrystals regardless of their size and doping concentration [Figs. 1(a) and S3]. SAXS size analysis using a spheroid fit indicates a marginal difference in nanocrystal core diameter between Sn_4-d_{11} and Sn_8-d_{11} (2.2%) and between Sn_4-d_{16} and Sn_8-d_{16} (3.5%) [Fig. 1(b) and Table I]. Dispersions of oleate-ITO display distinct LSPR absorption depending mainly on the tin doping content of nanocrystals

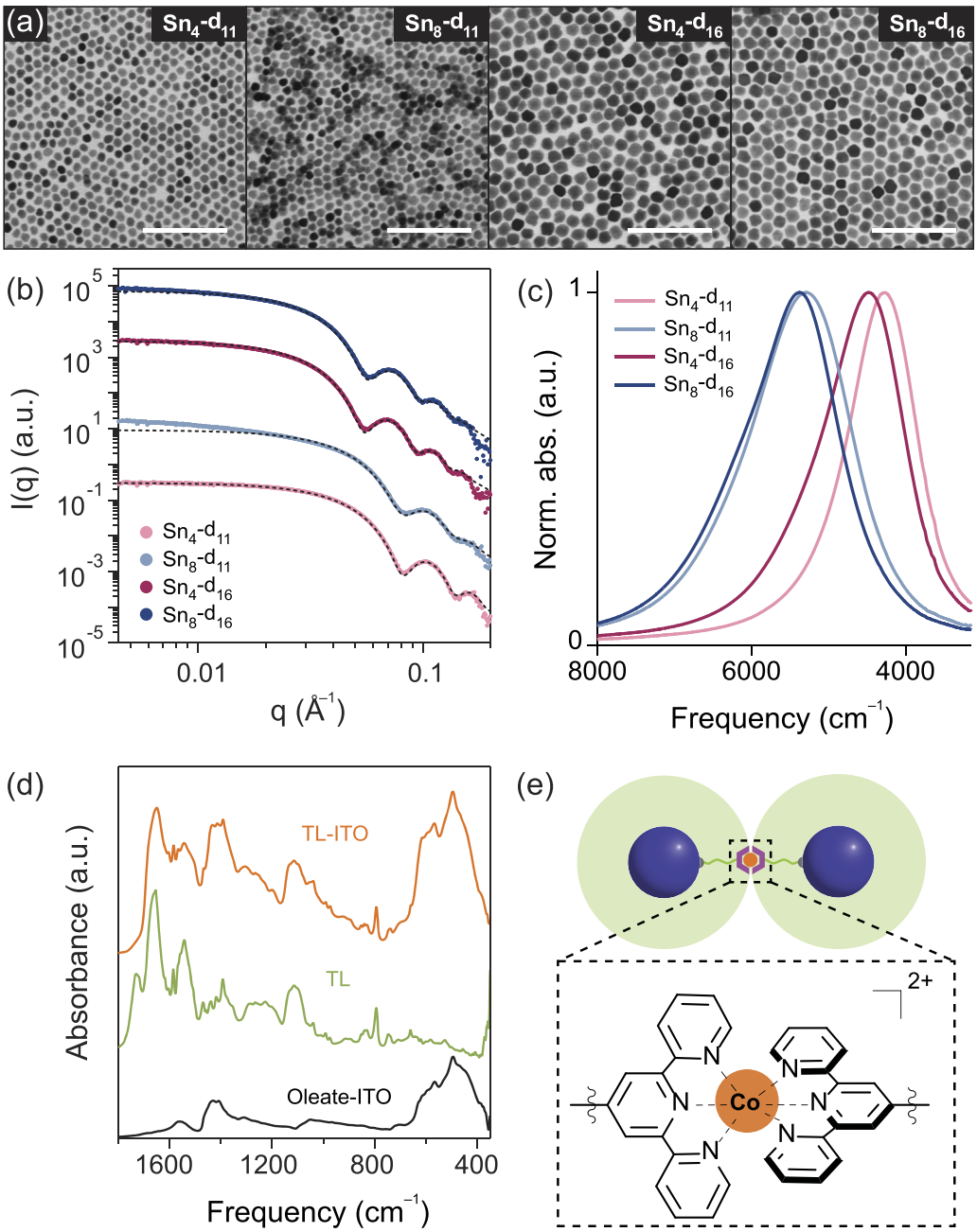

FIG. 1. Synthesis and ligand functionalization of ITO nanocrystals. (a) STEM images of oleate-ITO. Scale bars, 100 nm. (b) SAXS patterns (solid dots), offset for clarity, with spheroid fits (dashed lines) of oleate-ITO dispersions in hexane. (c) LSPR absorption spectra of oleate-ITO dispersions in tetrachloroethylene. (d) FTIR spectra of oleate-ITO, terpyridine-terminated ligand (**TL**), and **TL**-ITO. (e) Schematic of linking chemistry showing two nanocrystals (blue) connected via cobalt(II)–terpyridine coordination linkage.

[Fig. 1(c) and Table I], with LSPR peak frequencies of low-doped nanocrystals below 4500 cm^{-1} and those of high-doped ones above 5250 cm^{-1}. **TL**, consisting of a terpyridine functional domain, a polyethylene oxide ligand backbone, and a tricarboxylate binding group, was prepared via an established synthetic protocol (Figs. S1, S2, and S4) and used to functionalize oleate-ITO via direct ligand exchange.[29] Fourier-transform infrared spectroscopy (FTIR) establishes the presence of **TL** after ligand exchange [Fig. 1(d)]. The spectra of **TL**-ITO nanocrystals include characteristic peaks for terpyridine at 1605, 1566, and 790 cm^{-1}, representing ν(C=C) of the aromatic ring, ν(C=N) of pyridine, and ν(C–C) between pyridine rings, respectively. ν(C=O) of carboxylic acid at 1728 cm^{-1} observed in **TL** is absent for **TL**-ITO, implying **TL** is tethered to nanocrystals via the tricarboxylate binding group.

We have recently demonstrated that adding transition metal ions such as cobalt(II) can induce rapid, thermoreversible gelation of **TL**-ITO by forming metal–terpyridine coordination links [Figs. 1(e) and S5].[29] We have estimated the ITO volume fraction in the gels as 1.2%.[29] Similar to fast-forming hydrogels,[64] nanocrystal gels form within minutes, limited only by the time required to cool the system, in contrast with nanoparticle superlattices that typically require hours to days of annealing or slow cooling time to assemble.[65–67]

B. Well-mixed binary nanocrystal assembly

Adding Co^{2+} to two-component **TL**-ITO dispersions produced mixed nanocrystal gels without phase separating into single-component assemblies, even when the nanocrystal sizes were

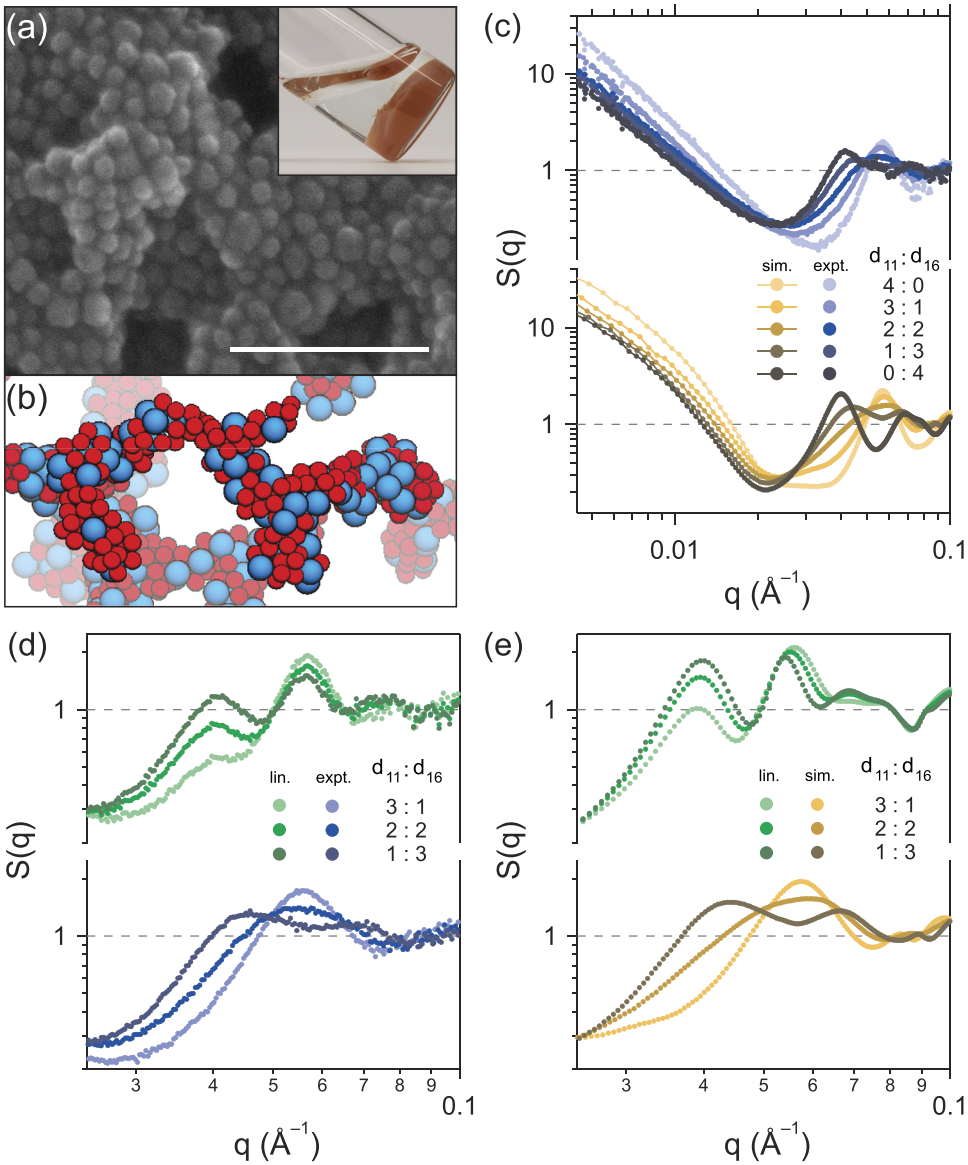

FIG. 2. Structure of mixed nanocrystal gels. (a) SEM image and photo (inset) of a nanocrystal gel comprising a 1:1 (v:v) mixture of Sn_4-d_{11} and Sn_4-d_{16}. Scale bar, 100 nm. (b) Snapshot of BD simulation showing a mixed nanocrystal assembly. (c) SAXS structure factor $S(q)$ of nanocrystal gels comprising 4:0, 3:1, 2:2, 1:3, and 0:4 (v:v) mixtures of Sn_4-d_{11} and Sn_4-d_{16} (top) and their simulated counterparts (bottom). (d) Zoomed-in view of the experimentally obtained $S(q)$ (bottom) and their calculated counterparts for hypothetical gels with no intermixing between different-sized nanocrystals (top). (e) Zoomed-in view of the simulated $S(q)$ (bottom) and their calculated counterparts for hypothetical gels with no intermixing between different-sized nanocrystals (top).

significantly different. Scanning electron microscopy (SEM) imaging of a dried gel comprising a 1:1 (v:v) mixture of Sn_4-d_{11} and Sn_4-d_{16} revealed that the nanocrystals with two disparate sizes are randomly interconnected, forming an open porous network [Figs. 2(a) and S6]. This intermixing is replicated in BD simulations using experimentally obtained nanocrystal sizes as input variables [Figs. 2(b) and S7]. The nanocrystal mixture separated into a gel phase that was colored a deep orange, a characteristic of the cobalt(II)–(bis)terpyridine links, and a clear supernatant after adding Co^{2+}, suggesting nearly all nanocrystals were incorporated in an extended gel network [Fig. 2(a), inset]. Random mixing of different-sized nanocrystals was evidenced by SAXS-based structural analysis of the resulting gel [Figs. 2(c), S8, and S9]. The structure factors $S(q)$ of gels containing Sn_4-d_{11} and Sn_4-d_{16} in different volume ratios were obtained by dividing the SAXS pattern of a mixed gel by that of a dispersion with the same mixing ratio. Regardless of the nanocrystal mixing ratio, gels exhibited diverging $S(q)$ at low q with a fractal dimension of 2.3–2.5, indicating consistent mesoscale organization of mixed nanocrystal assemblies.

The high q region of $S(q)$ showed signatures of random mixing between different-sized nanocrystals [Fig. 2(d)]. While the calculated $S(q)$ for hypothetical gels with no intermixing between the components showed distinct peaks at 0.042 and 0.057 $Å^{-1}$, indicative of the characteristic lengths in the single-component assemblies of Sn_4-d_{16} and Sn_4-d_{11}, respectively, the experimentally obtained $S(q)$ patterns exhibited broad peaks *between* the two q values, suggesting random mixing of different-sized nanocrystals in gels. The q range of these broad peaks and the shifting peak maxima with mixing ratio reflect the distribution of nanocrystal spacings present due to the intermixing of small and large nanocrystals. To confirm this interpretation of the experimental SAXS patterns, similar structural analysis was performed on BD simulations of mixed nanocrystal gels. Using thermodynamic nanocrystal sizes determined solely from single-component gels, the experimental trends of $S(q)$ were qualitatively reproduced with mixed nanocrystal BD simulations, validating our simulation model for randomly-mixed nanocrystal gel assemblies and supporting the interpretation of the experimental results [Figs. 2(c) and 2(e)]. Mixed nanocrystal gels containing Sn_8-d_{11} and Sn_8-d_{16} also exhibited the identical trends (Fig. S9), while gels composed of the same-sized nanocrystals displayed nearly constant $S(q)$ in the high q region regardless of mixing ratio (Fig. S10). This facile mixing contrasts with the precise size matching required to produce randomly mixed, multi-component superlattices[41,68] and presents an opportunity to maximize synergistic coupling in multi-component nanocrystal gel assemblies.

C. Infrared response of mixed nanocrystal gels

The optical response of the mixed nanocrystal dispersion switches abruptly upon gelation, and the spectra can be consistently reproduced on temperature cycling between the dispersion and gel states, confirming mixing is reliably achieved and properties can be rationally tuned by adjusting components and their mixing ratio (Fig. 3). Due to the highly reversible nature of the metal coordination linkage used,[29] a two-component nanocrystal assembly consisting of Sn_4-d_{11} and Sn_8-d_{16} showed consistent LSPR absorption spectra in both dispersion (at 90 °C) and gel (at 20 °C) states, demonstrated over five thermal cycles. Although the spectral contributions of the

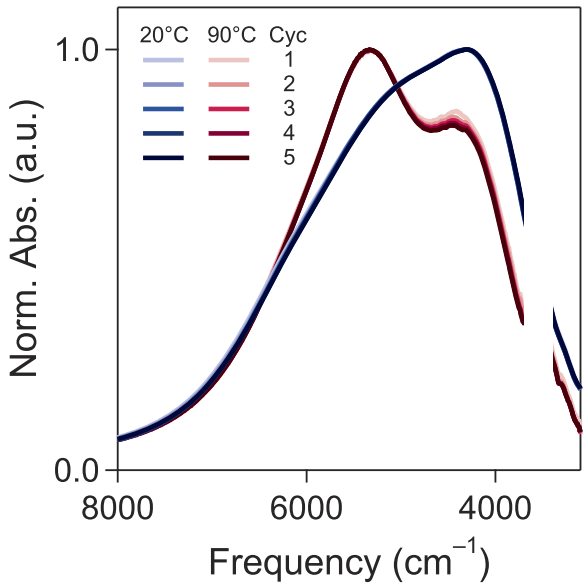

FIG. 3. Reproducible optical spectra of mixed nanocrystal gels. LSPR absorption spectra of a thermoreversible nanocrystal assembly comprising a 1:1 (v:v) mixture of Sn_4-d_{11} and Sn_8-d_{16} over five thermal cycles between dispersion and gel states. For clarity, the spectral region for ν(O–H) absorption is not shown.

two nanocrystal components are apparent in both the dispersion and gel states, their relative strength changes upon assembly. As a result, the peak maximum undergoes a large shift from 5332 cm^{-1} in the mixed nanocrystal dispersion to 4307 cm^{-1} in the gel, a shift of 1025 cm^{-1}. This optical modulation is large compared to the shift of about 500 cm^{-1} we previously observed in single-component ITO nanocrystal gel assemblies, demonstrating just one example of how multicomponent ITO gels can give rise to unique properties.

The optical spectra of two-component mixed nanocrystal gels were similar to the weighted sum of the respective single-component gels, but they also exhibited signatures of cross-coupling between nanocrystals with distinct LSPR absorption, most noticeably near 1:1 (v:v) mixing ratios. Infrared absorption spectra were measured for gels with different mixing ratios of nanocrystals that have the same size but distinct LSPR responses, while the overall volume fraction of nanocrystals in each sample was fixed at 0.1% [Figs. 4(a) and 4(d)]. LSPR absorption spectra of mixed gels evolved gradually to higher energy as the volume fraction of 8% Sn nanocrystals increased, demonstrating continuous optical tuning of gel assemblies by modular mixing of plasmonic nanocrystals. Note that the absorption peak at 3540 cm^{-1} is due to the O–H stretching of residual ethanol used to wash nanocrystals or ambient water. The collective infrared response of mixed gels approximately reflects the volume-weighted average spectra of the two single-component assemblies with some systematic deviations [Figs. 4(b) and 4(e)]. Compared to expectations based on linear mixing, a two-component gel comprising a 1:3 (v:v) mixture of Sn_4-d_{11} and Sn_8-d_{11} showed a blueshifted peak at a higher frequency and a redshifted shoulder at a lower frequency [Fig. 4(b)]. Similarly, a gel with the opposite mixing ratio (3:1) exhibited a blueshifted shoulder at higher frequency and a redshifted peak

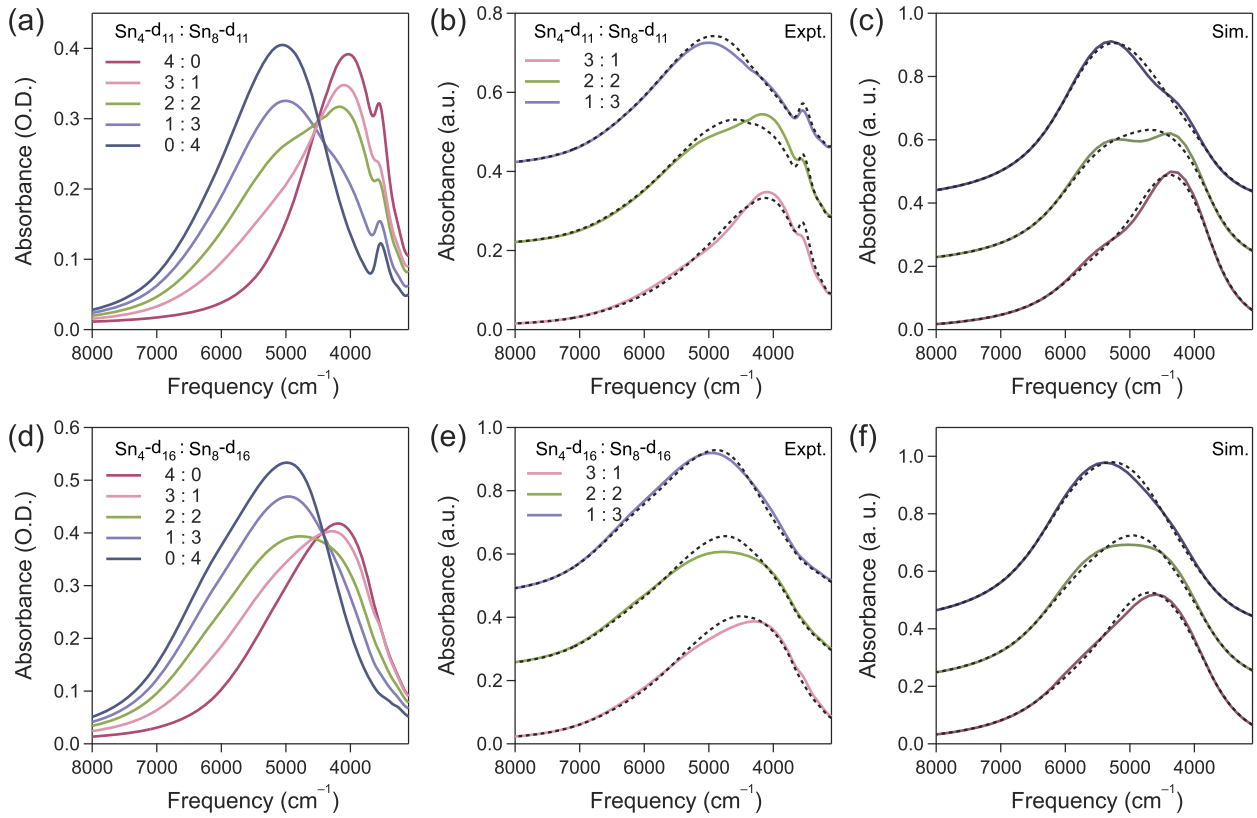

FIG. 4. Infrared absorption of mixed nanocrystal gels comprising ITO nanocrystals with the same size and different tin doping concentration. LSPR absorption spectra of nanocrystal gels comprising 4:0, 3:1, 2:2, 1:3, and 0:4 (v:v) mixtures of (a) Sn_4-d_{11} and Sn_8-d_{11} and (d) Sn_4-d_{16} and Sn_8-d_{16}. (b) and (e) LSPR absorption spectra of mixed nanocrystal gels (solid) and their calculated counterparts, assuming no intermixing between the two different types of nanocrystals (dashed). (c) and (f) Simulated extinction spectra of mixed nanocrystal gels (solid) and their calculated counterparts, assuming no intermixing between the two different types of nanocrystals (dashed).

at lower frequency than expected. The deviations are more obvious at the 1:1 mixing ratio, where contributions from the two component nanocrystals are balanced, resulting in two discernible spectral components instead of the single broad peak expected from simple linear mixing. In all cases, the spectral contributions from the component nanocrystals are more distinct in mixed gels than they would be in a macrophase-separated mixture of two single-component gels.

These trends in the far-field responses were qualitatively reproduced in simulations of gel extinction using MPM [Fig. 4(c)]. To simulate the gel spectra without free parameters, we used thermodynamic sizes derived from experimental SAXS patterns, as described in Sec. II, and parameters defining the ITO nanocrystals' dielectric functions found by analysis of experimental LSPR spectra for dilute dispersions of each nanocrystal type. Because the infrared LSPR of ITO nanocrystals is far from other optical transitions, like bandgap absorption that lies in the ultraviolet, the dielectric function of the nanocrystals is well represented by a damped free electron (Drude) model over the relevant frequency range. The plasmonic core is surrounded by a depletion layer, where band bending induces a very low electron concentration, which we model as a dielectric shell.[69] Fitting the extinction spectra of dilute dispersions of each nanocrystal type,[63] we determine the dielectric function parameters for the plasmonic core and depletion layer (Fig. S11 and Table S2), which are then held fixed when simulating the optical response of the single- and two-component gels. Simulated gel spectra show blueshifted peaks or shoulders at a higher frequency and redshifted counterparts at a lower frequency compared to expectations based on simple linear mixing. Mixed gels comprising Sn_4-d_{16} and Sn_8-d_{16} showed similar spectral trends to the gels fabricated from the smaller nanocrystals in both experiments and simulations, exhibiting blueshifted high-frequency and redshifted low-frequency features in the LSPR absorption spectra at different mixing ratios compared to the single broadened peak expected for all compositions based on linear mixing [Figs. 4(d)–4(f)].

Random mixing of components using our linking strategy also led to mixing-tunable optical spectra with signs of cross-coupling when different-sized nanocrystals were co-assembled. Consistent with the well-mixed nanocrystal structure ascertained by SAXS analysis [Fig. 2(c)], mixed gels composed of Sn_4-d_{11} and Sn_8-d_{16} and those composed of Sn_4-d_{16} and Sn_8-d_{11} displayed infrared absorption spectra that resemble the sum of single-component gels, but with consistent deviating characteristics [Figs. 5(a), 5(b), 5(d),

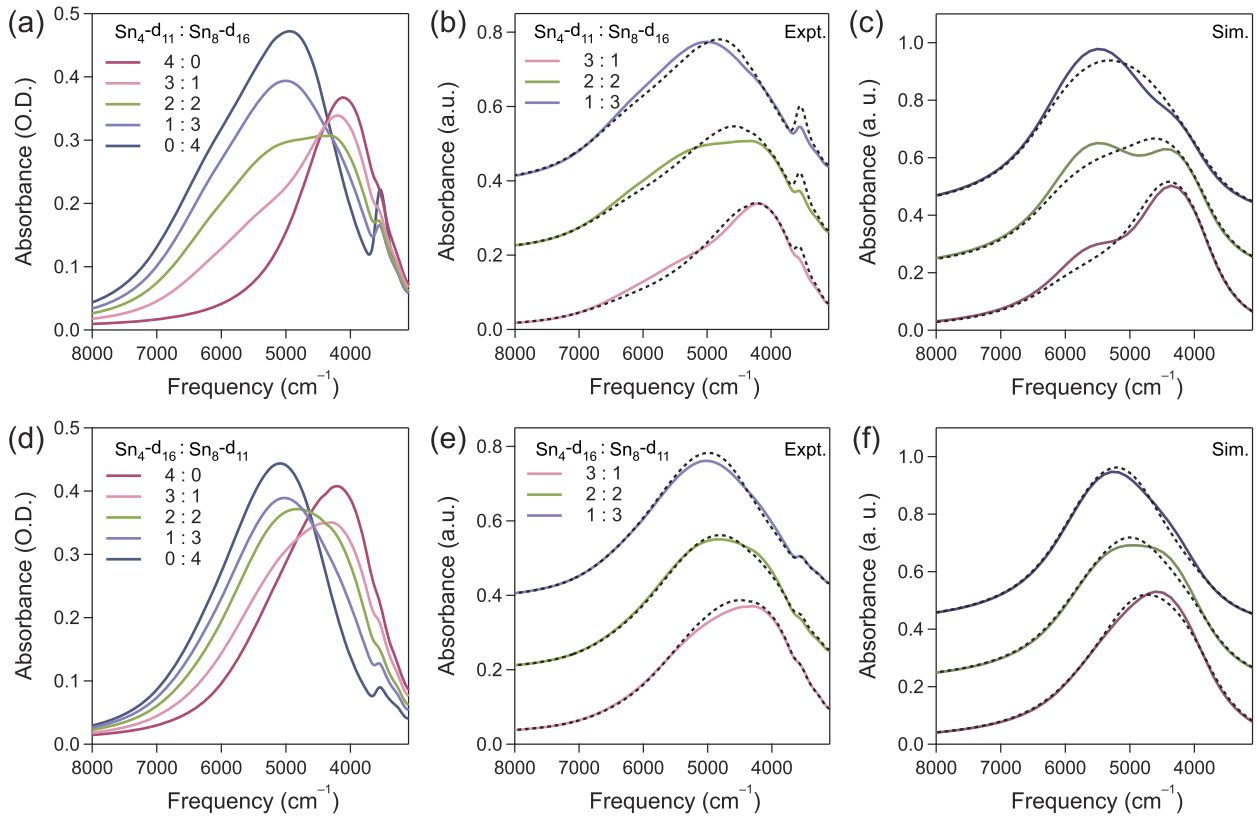

FIG. 5. Infrared response of mixed nanocrystal gels comprising ITO nanocrystals with different sizes and tin doping concentrations. LSPR absorption spectra of nanocrystal gels comprising 4:0, 3:1, 2:2, 1:3, and 0:4 (v:v) mixtures of (a) Sn_4-d_{11} and Sn_8-d_{16} and (d) Sn_4-d_{16} and Sn_8-d_{11}. (b) and (e) LSPR absorption spectra of mixed nanocrystal gels (solid) and their calculated counterparts assuming no intermixing between the two types of nanocrystals (dashed). (c) and (f) Simulated extinction spectra of mixed nanocrystal gels (solid) and their calculated counterparts, assuming no intermixing between the two types of nanocrystals (dashed).

and 5(e)]. Similar to mixed gels comprising same-sized nanocrystals, the blueshifting of high-frequency peaks (or shoulders) and the redshifting of low-frequency peaks (or shoulders) were again observed, indicating cross-coupling between different-sized plasmonic nanocrystals leads to more distinct spectral contributions from each component in the randomly mixed gels. These spectral trends were reproduced using MPM simulations, further supporting our SAXS analysis that the constituent nanocrystals are well-mixed in gel assemblies [Figs. 5(c) and 5(f)]. Infrared spectra of co-assembled nanocrystals with the same doping concentration and different sizes were also collected (Fig. S12); the nearly resonant LSPR peaks of the two plasmonic nanocrystals made it difficult to discern any effects of cross-coupling in those cases.

D. Near- and far-field analysis of mixed nanocrystal gels using MPM

To understand the mechanisms underlying the coupling effects observed in far-field spectra, both near- and far-field properties of mixed gels were assessed using MPM (Figs. 6, 7, and S13–S26). From both experiments and simulations, mixed gels composed of nanocrystals with dissimilar LSPR frequencies consistently evinced sharper component extinction peaks than the weight-averaged spectra of the single component gels [Figs. 4–6(a)]. MPM allows the contributions of each nanocrystal component to the spectra to be separately evaluated as a function of the mixing ratio. If the extinction spectra of mixed gels were accurately described by the linear superposition of pure gels, these component spectra would be independent of the mixing ratio. However, compared to the single-component Sn_8-d_{16} gel, the high-frequency component gradually blueshifts and sharpens as these nanocrystals are mixed with increasing amounts of Sn_4-d_{11} [Fig. 6(b)]. Likewise, the low-frequency component arising from Sn_4-d_{11} redshifts and gains an extinction cross section when mixed with Sn_8-d_{16}, resulting in a sharpened low-frequency LSPR component in mixed gels [Fig. 6(c)]. Monitoring the peak features of the simulated extinction cross sections offers a more evident view of the spectral evolution of the mixed gels [Figs. 6(d)–6(f)]. The peak position (ω_{LSPR}) of the high-frequency (low-frequency) component continuously blueshifts (redshifts) with dilution [Fig. 6(d)], while the full width at half maximum (FWHM) of both components decreases (indicating sharpening) with dilution compared to the spectra of single-component gels [Fig. 6(f)].

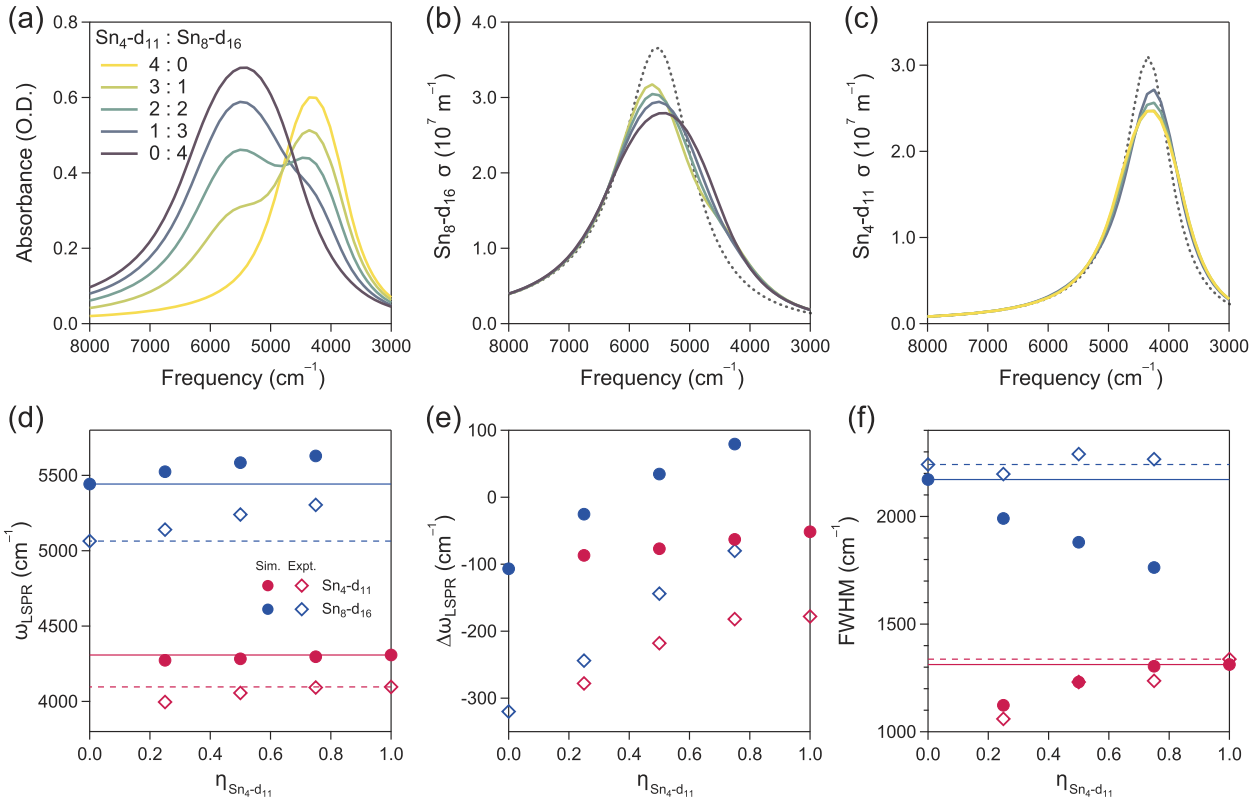

FIG. 6. Far-field analysis of LSPR in mixed nanocrystal gels. (a) Simulated extinction spectra of mixed nanocrystal gels comprising Sn_4-d_{11} and Sn_8-d_{16} at different mixing ratios. (b) and (c) Extinction cross section σ of the component nanocrystals, (b) Sn_8-d_{16} and (c) Sn_4-d_{11}, per volume of ITO at different mixing ratios. The extinction cross section of an isolated nanocrystal of each type is shown as a dotted line for comparison. (d) Peak position (ω_{LSPR}), (e) shift in peak position ($\Delta\omega_{LSPR}$) relative to the corresponding nanocrystal dispersion, and (f) full width at half maximum (FWHM) of the high (Sn_8-d_{16}, filled blue circle) and low (Sn_4-d_{11}, filled red circle) frequency component nanocrystal extinction cross sections from simulation, and of the high (hollow blue diamond) and low (hollow red diamond) frequency spectral contributions deconvoluted from the experimental data at different mixing fractions of Sn_4-d_{11} (ηSn_4-d_{11}). ω_{LSPR} and FWHM of single-component nanocrystal gels are marked with horizontal colored lines for clarity (solid for simulation results, dashed for experimental).

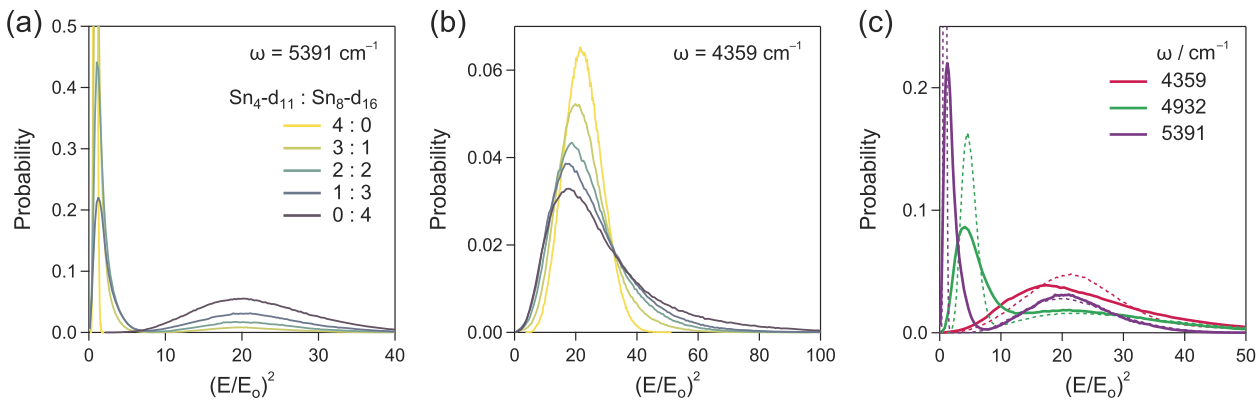

FIG. 7. Near-field analysis of LSPR in mixed nanocrystal gels. Near-field hotspot intensity distributions of mixed nanocrystal gels comprising Sn_4-d_{11} and Sn_8-d_{16} at (a) the high-frequency LSPR for a pure Sn_8-d_{16} gel and (b) the low-frequency LSPR for a pure Sn_4-d_{11} gel. (c) Near-field distributions of a mixed gel comprising a 1:1 (v:v) mixture of Sn_4-d_{11} and Sn_8-d_{16} at different frequencies (solid) and their simple linear mixing counterparts (dashed).

Interestingly, ω_{LSPR} of the high-frequency component blueshifts even beyond the peak position of an isolated nanocrystal when the mixing fraction of the low-frequency component (ηSn_4-d_{11}) is greater than about 0.5 [Fig. 6(e)]. This shift occurs without any change in the electronic structure (e.g., electron concentration) of the component nanocrystals and must be attributed to the evolving environment for LSPR coupling as the mixing fraction changes. The same qualitative trends in ω_{LSPR} and FWHM were consistently reproduced with mixed gels comprising high- and low-doped nanocrystals with different combinations of nanocrystal size (Figs. S13–S15), whereas mixed gels comprising nanocrystals with the same doping concentration manifested less obvious trends in peak features due to the proximity of the peak positions (Figs. S16 and S17).

The evolving peak features at different mixing ratios were qualitatively reproduced in the high- and low-frequency contributions to the experimental spectra of mixed gels deconvoluted via an exponentially modified Gaussian distribution (EMG) fit [Figs. 6(d)–6(f) and S13–S23]. The deconvoluted spectra of the high- and low-frequency components likewise generally display blueshifting and redshifting peak positions, respectively, with dilution, although the narrowing FWHM was less apparent. Unlike the simulated spectral components, the deconvoluted experimental components capture all spectral signals in the high- or low-frequency regions without respect to the type of nanocrystal giving rise to the absorption, likely accounting for the differences in line shape trends between simulated and experimental results.

The shifting of the component peaks can be rationalized by the changing LSPR coupling environment with a mixing ratio. As the fraction of low energy particles increases in mixed gels, high energy particles are surrounded by fewer near-resonant particles, leading to weaker LSPR coupling and reduced redshifting of the high-energy peak compared to the dispersion. In the simulations, where the specific contribution of the high energy nanocrystals can be isolated, their peak can be higher energy than even an isolated nanocrystal when well-diluted with lower frequency NCs. This unusual coupling effect may depend on the specific gel structure and bears further investigation. In contrast, low energy particles couple strongly with both resonant and off-resonant, high energy neighbors, where strong coupling with the latter nanocrystals results in increased redshifting of the low energy component with dilution.

Besides tunable absorption spectra, assemblies of plasmonic nanocrystals give rise to hot spots where the electric field of the incoming light is strongly enhanced, especially in gaps between closely spaced nanocrystals. The resonance condition of neighboring nanocrystals, and hence the compositional mixing in multicomponent gels, is expected to influence the magnitude of the near-field enhancement (NFE) throughout the gel. Here, NFE is the factor by which the local electric field intensity is enhanced compared to the intensity of incident light, NFE = $(E/E_0)^2$. From MPM simulations, we found the local intensity maximum of the NFE at the hot spots on the surface of each nanocrystal and compared the probability distributions of these values in single-component and mixed gels at the varying excitation frequencies. In a mixed gel comprising a mixture of Sn_4-d_{11} and Sn_8-d_{16}, for example, changing the mixing ratio has a qualitatively different effect on the NFE around the two types of nanocrystals. First examining excitation at high frequency, the probability of intense hot spots continuously diminishes as resonant Sn_8-d_{16} nanocrystals are diluted with off-resonant Sn_4-d_{11} [Fig. 7(a)]. The lower frequency nanocrystals effectively act as dielectric spacers, reducing the prevalence of pairs of Sn_8-d_{16} that can create intense hot spots. A second population of very weak hot spots emerges, producing a bimodal distribution of hotspot intensities. Conversely, for low-frequency excitation, the hot spots around resonant Sn_4-d_{11} nanocrystals persist as they are diluted with Sn_8-d_{16}, since the higher doping concentration nanocrystals also effectively couple with the lower doped component particles [Fig. 7(b)]. Analogous observations regarding hotspot intensity distributions were made using MPM analysis in ordered superlattices of mixed ITO nanocrystals.[53]

The NFE distributions are broadened for mixed gels owing to local compositional heterogeneity. Compared to the NFE distributions for a linear combination of single-component gels, the wider distribution of hotspot intensities in the same composition 1:1 mixed gel is apparent for low-frequency excitation [Fig. 7(c), red lines]. Hence, the distribution reflects not just a mixing of components but a mixing of diverse local environments as high- and low-doping concentration nanocrystals interact to form a wide range of hot spots in the mixed gel. Even for high-frequency excitation, mixing creates hot spots with non-negligible NFE around the off-resonant nanocrystals, and the intensity distribution is broadened around the low NFE peak [Fig. 7(c), purple lines]. Even at intermediate frequencies, the mixed nanocrystal gels have a broader distribution of near-field intensities than pure component gels. When varying the structure of single-component nanocrystal gels, the far-field extinction and hot-spot intensity distributions broaden together,[31] so the simultaneous sharpening of contributions to the extinction peak and broadening of near-field intensity distributions is a unique feature of mixed nanocrystal gels.

E. Co-assembly of nanocrystals with different shapes

Besides different sizes and doping concentrations, nanocrystals with different shapes can also be incorporated into mixed gel assemblies. During nanocrystal synthesis, adding fluorine as a co-dopant with tin results in cube-shaped fluorine, tin co-doped indium oxide (FITO) nanocrystals, as previously reported.[56] Bright-field STEM images show monodisperse, cubic FITO nanocrystals with an average edge length of 13.2 nm [Figs. 8(a) and S3]. When assembled into a single-component gel, FITO nanocrystals formed an open porous network without any ordered arrangement or apparent orientational alignment between neighboring nanocubes [Figs. 8(b) and S28]. To assess LSPR coupling in FITO gel assemblies, infrared absorption spectra of **TL**-FITO dispersions containing Co^{2+} and excess Cl^- were collected *in situ* at different temperatures [Fig. 8(c)]. The LSPR absorption spectrum of FITO nanocubes can be deconvoluted into contributions from the face, edge, and corner modes at distinct frequencies, in decreasing order; the peak maximum is dominated by the corner mode (Fig. S27). In the nanocrystal-linker solution, above 70 °C, the spectrum is almost identical to that of the **TL**-FITO dispersion before adding the metal ion linker (Co^{2+}), showing that nanocubes are fully dispersed. As the temperature decreased below 70 °C, however, the absorption spectrum was abruptly redshifted and broadened due to LSPR coupling in the nanocrystal assembly. The absorption contribution from the corner mode showed a particularly significant redshifting from above 5000 cm^{-1} to below

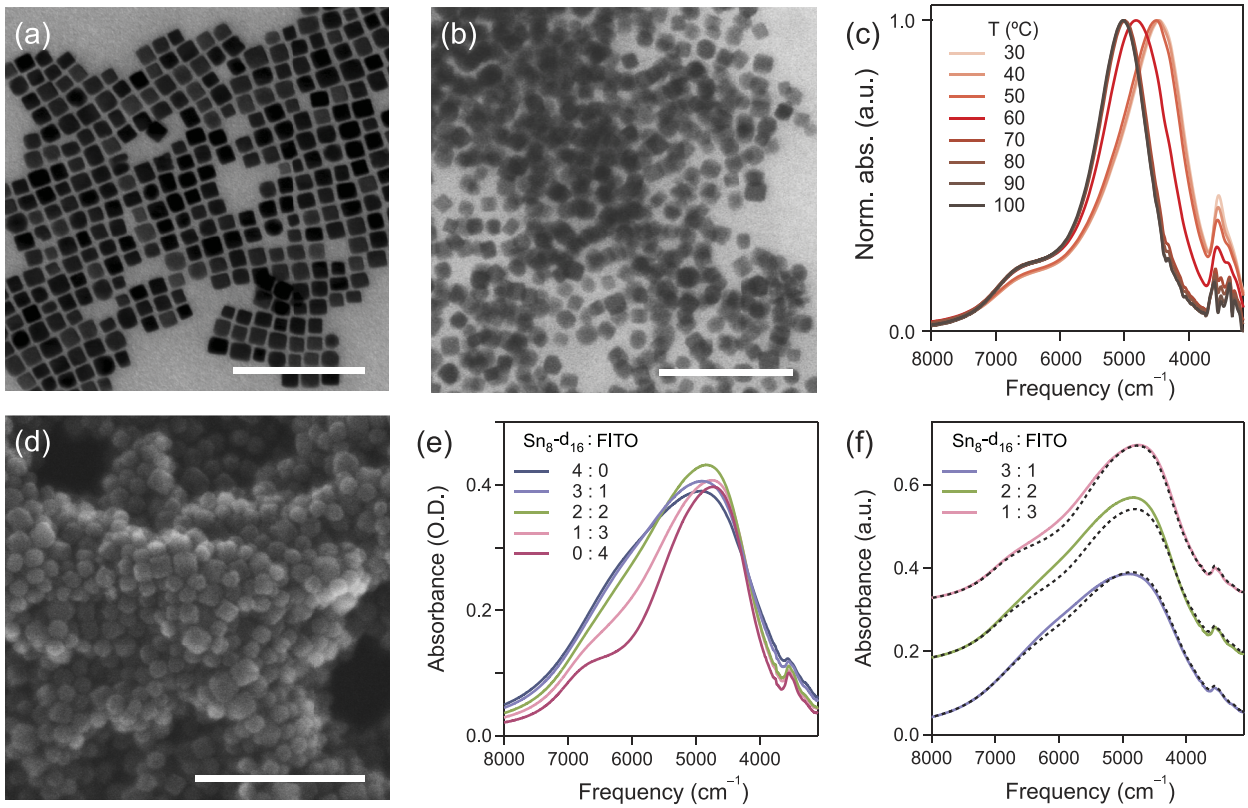

FIG. 8. Mixed nanocrystal gels comprising FITO nanocubes and ITO nanospheres. STEM images of (a) oleate-FITO nanocubes and (b) a nanocrystal gel comprising **TL**-FITO nanocubes (**TL**-FITO). (c) LSPR absorption spectra of a thermoreversible nanocube assembly in DMF at varying temperatures. (d) SEM image of a nanocrystal gel comprising a 1:1 (v:v) mixture of **TL**-FITO (13.2 nm edge length) and **TL**-ITO (10.4 nm diameter). Scale bars, 100 nm. (e) LSPR absorption spectra of nanocrystal gels made of 4:0, 3:1, 2:2, 1:3, and 0:4 (v:v) mixtures of Sn_8-d_{16} nanospheres and Sn_6-d_{13} nanocubes. (f) LSPR absorption spectra of mixed nanocrystal gels (solid) and their calculated counterparts, assuming no intermixing between the two different nanocrystals (dashed).

4500 cm^{-1}, exceeding the ~500 cm^{-1} shift observed previously in ITO nanosphere gels[29] and indicating strong LSPR coupling. The co-assembly of different-sized nanocubes and nanospheres using metal–terpyridine links proceeds readily with a randomly mixed configuration of the two components in the resulting gel assemblies [Figs. 8(d) and S28]. The collective LSPR spectra of mixed nanosphere-nanocube gels exhibited slightly increased absorption on the high-frequency side of the peak, at around 6000 cm^{-1}, compared to simple linear mixing, again suggesting some cross-coupling between different-shaped plasmonic nanocrystals [Figs. 8(e) and 8(f)].

IV. CONCLUSIONS

Gelation mediated by thermoreversible metal–terpyridine links enables the modular incorporation of nanocrystals regardless of their size, doping concentration, and shape. By simply varying the mixing ratio, we showed both the far- and near-field optical properties of two-component ITO nanocrystal gels that can be tuned more broadly than in single-component gel networks. Emergent optical properties deviating from simple linear mixing suggest cross-coupling between distinct plasmonic nanocrystals in gel assemblies. We expect this strategy to be applicable to make multi-component assemblies also incorporating metal nanoparticles, semiconductor quantum dots, and other nanoscale components of interest, allowing synergistic properties such as plasmon-enhanced absorption or emission or directed energy or electron transfer. Reliable, reproducible mixing of assembled components using thermoresponsive links opens the door to switchable materials with properties that are deliberately varied by changing mixing ratios, while other responsive linking strategies could be devised to disassemble and reassemble according to optical or chemical stimuli. In other gelation strategies where nanocrystal linking rates vary with the composition of the inorganic core, chemical rebalancing of kinetics controls whether nanocrystals are mixed or phase separated.[49] In our case, the universal linking strategy promotes consistent intermixing, while control over spatial variation of composition may be introduced in the future work by leveraging the orthogonality between metal–terpyridine links and other dynamic covalent bonding chemistries.[70] For example, we can envision multi-component nanocrystal assemblies programmed to reconfigure with specificity, e.g., by enforcing alternate placement of high- and

low-doping concentration ITO nanocrystals in response to different types of stimuli (chemicals, light, heat, strain, etc.). Modular mixing of linkers or ligands with different lengths, rigidities, or other characteristics can also be envisioned to template structure and direct structure-dependent properties of nanocrystal assemblies.[26,31]

SUPPLEMENTARY MATERIAL

See the supplementary material for synthetic protocol and characterization of **TL** and nanocrystals (LCMS, STEM images, and SAXS patterns) and description on the MPM model and simulations.

ACKNOWLEDGMENTS

This research was primarily supported by the National Science Foundation through the Center for Dynamics and Control of Materials: an NSF MRSEC under Cooperative Agreement No. DMR-1720595, with additional support from an Arnold O. Beckman Postdoctoral Fellowship (Z.M.S.) and the Welch Foundation (Grant Nos. F-1696 and F-1848). E.V.A. acknowledges support from the Welch Regents Chair (No. F-0046). We acknowledge the Texas Advanced Computing Center (TACC) at the University of Texas at Austin for providing HPC resources.

AUTHOR DECLARATIONS

Conflict of Interest

The authors have no conflicts to disclose.

Author Contributions

Jiho Kang: Conceptualization (lead); Data curation (lead); Formal analysis (lead); Investigation (lead); Visualization (lead); Writing – original draft (lead); Writing – review & editing (lead). **Zachary M. Sherman**: Conceptualization (lead); Data curation (lead); Formal analysis (lead); Investigation (lead); Software (lead); Visualization (equal); Writing – original draft (lead); Writing – review & editing (lead). **Hannah S. N. Crory**: Data curation (equal); Formal analysis (equal); Visualization (equal); Writing – original draft (equal); Writing – review & editing (supporting). **Diana L. Conrad**: Data curation (equal); Formal analysis (supporting); Writing – review & editing (supporting). **Marina W. Berry**: Data curation (supporting); Writing – original draft (supporting); Writing – review & editing (supporting). **Benjamin J. Roman**: Formal analysis (supporting); Investigation (equal); Writing – review & editing (supporting). **Eric V. Anslyn**: Funding acquisition (lead); Supervision (equal); Writing – review & editing (equal). **Thomas M. Truskett**: Conceptualization (lead); Funding acquisition (lead); Project administration (lead); Supervision (lead); Writing – original draft (equal); Writing – review & editing (lead). **Delia J. Milliron**: Conceptualization (lead); Funding acquisition (lead); Project administration (lead); Supervision (lead); Writing – original draft (lead); Writing – review & editing (lead).

DATA AVAILABILITY

The data that support the findings of this study are available from the corresponding author upon reasonable request.

REFERENCES

[1] S. V. Gaponenko, *Optical Properties of Semiconductor Nanocrystals* (Cambridge University Press, 1998), Vol. 23.
[2] S. Link and M. A. El-Sayed, "Optical properties and ultrafast dynamics of metallic nanocrystals," Annu. Rev. Phys. Chem. **54**, 331–366 (2003).
[3] V. Giannini, A. I. Fernández-Domínguez, S. C. Heck, and S. A. Maier, "Plasmonic nanoantennas: Fundamentals and their use in controlling the radiative properties of nanoemitters," Chem. Rev. **111**, 3888–3912 (2011).
[4] A. Agrawal, S. H. Cho, O. Zandi, S. Ghosh, R. W. Johns, and D. J. Milliron, "Localized surface plasmon resonance in semiconductor nanocrystals," Chem. Rev. **118**, 3121–3207 (2018).
[5] J. Shamsi, A. S. Urban, M. Imran, L. De Trizio, and L. Manna, "Metal halide perovskite nanocrystals: Synthesis, post-synthesis modifications, and their optical properties," Chem. Rev. **119**, 3296–3348 (2019).
[6] R. Fu, S. Liu, Q. Shi, Y. Lu, Z. Yong, and W. Cheng, "Active strain engineering of soft plasmene nanosheets by thermoresponsive hydrogels," J. Mater. Chem. C **9**, 12720–12726 (2021).
[7] S. Wang, Y. Zhang, X. Qin, L. Zhang, Z. Zhang, W. Lu, and M. Liu, "Guanosine assembly enabled gold nanorods with dual thermo- and photoswitchable plasmonic chiroptical activity," ACS Nano **14**, 6087–6096 (2020).
[8] X. Wang, D. Xu, B. Jaquet, Y. Yang, J. Wang, H. Huang, Y. Chen, C. Gerhard, and K. Zhang, "Structural colors by synergistic birefringence and surface plasmon resonance," ACS Nano **14**, 16832–16839 (2020).
[9] X. Wen, H. Fan, L. Jing, M. Deng, X. Huang, T. Jiao, L. Zhang, and M. Liu, "Competitive induction of circularly polarized luminescence of CdSe/ZnS quantum dots in a nucleotide–amino acid hydrogel," Mater. Adv. **3**, 682–688 (2022).
[10] I. U. Arachchige and S. L. Brock, "Sol–gel methods for the assembly of metal chalcogenide quantum dots," Acc. Chem. Res. **40**, 801–809 (2007).
[11] N. Gaponik, A.-K. Herrmann, and A. Eychmüller, "Colloidal nanocrystal-based gels and aerogels: Material aspects and application perspectives," J. Phys. Chem. Lett. **3**, 8–17 (2011).
[12] F. Matter, A. L. Luna, and M. Niederberger, "From colloidal dispersions to aerogels: How to master nanoparticle gelation," Nano Today **30**, 100827 (2020).
[13] Z. M. Sherman, A. M. Green, M. P. Howard, E. V. Anslyn, T. M. Truskett, and D. J. Milliron, "Colloidal nanocrystal gels from thermodynamic principles," Acc. Chem. Res. **54**, 798–807 (2021).
[14] A. M. Green, C. K. Ofosu, J. Kang, E. V. Anslyn, T. M. Truskett, and D. J. Milliron, "Assembling inorganic nanocrystal gels," Nano Lett. **22**, 1457–1466 (2022).
[15] A. B. Pawar and I. Kretzschmar, "Fabrication, assembly, and application of patchy particles," Macromol. Rapid Commun. **31**, 150–168 (2010).
[16] W. Li, H. Palis, R. Mérindol, J. Majimel, S. Ravaine, and E. Duguet, "Colloidal molecules and patchy particles: Complementary concepts, synthesis and self-assembly," Chem. Soc. Rev. **49**, 1955–1976 (2020).
[17] B. A. Lindquist, R. B. Jadrich, D. J. Milliron, and T. M. Truskett, "On the formation of equilibrium gels via a macroscopic bond limitation," J. Chem. Phys. **145**, 074906 (2016).
[18] A. Singh, B. A. Lindquist, G. K. Ong, R. B. Jadrich, A. Singh, H. Ha, C. J. Ellison, T. M. Truskett, and D. J. Milliron, "Linking semiconductor nanocrystals into gel networks through all-inorganic bridges," Angew. Chem., Int. Ed. **54**, 14840–14844 (2015).
[19] V. Sayevich, B. Cai, A. Benad, D. Haubold, L. Sonntag, N. Gaponik, V. Lesnyak, and A. Eychmüller, "3D assembly of all-inorganic colloidal nanocrystals into gels and aerogels," Angew. Chem., Int. Ed. **55**, 6334–6338 (2016).
[20] M. P. Howard, R. B. Jadrich, B. A. Lindquist, F. Khabaz, R. T. Bonnecaze, D. J. Milliron, and T. M. Truskett, "Structure and phase behavior of polymer-linked colloidal gels," J. Chem. Phys. **151**, 124901 (2019).
[21] F. Bomboi, D. Caprara, J. Fernandez-Castanon, and F. Sciortino, "Cold-swappable DNA gels," Nanoscale **11**, 9691–9697 (2019).
[22] J. Lowensohn, B. Oyarzún, G. N. Paliza, B. M. Mognetti, and W. B. Rogers, "Linker-mediated phase behavior of DNA-coated colloids," Phys. Rev. X **9**, 041054 (2019).
[23] M. N. Dominguez, M. P. Howard, J. M. Maier, S. A. Valenzuela, Z. M. Sherman, J. F. Reuther, L. C. Reimnitz, J. Kang, S. H. Cho, S. L. Gibbs, A. K. Menta,

D. L. Zhuang, A. van der Stok, S. J. Kline, E. V. Anslyn, T. M. Truskett, and D. J. Milliron, "Assembly of linked nanocrystal colloids by reversible covalent bonds," Chem. Mater. **32**, 10235–10245 (2020).

[24]J. Song, M. H. Rizvi, B. B. Lynch, J. Ilavsky, D. Mankus, J. B. Tracy, G. H. McKinley, and N. Holten-Andersen, "Programmable anisotropy and percolation in supramolecular patchy particle gels," ACS Nano **14**, 17018–17027 (2020).

[25]M. P. Howard, Z. M. Sherman, D. J. Milliron, and T. M. Truskett, "Wertheim's thermodynamic perturbation theory with double-bond association and its application to colloid–linker mixtures," J. Chem. Phys. **154**, 024905 (2021).

[26]M. P. Howard, Z. M. Sherman, A. N. Sreenivasan, S. A. Valenzuela, E. V. Anslyn, D. J. Milliron, and T. M. Truskett, "Effects of linker flexibility on phase behavior and structure of linked colloidal gels," J. Chem. Phys. **154**, 074901 (2021).

[27]R. Braz Teixeira, D. de Las Heras, J. M. Tavares, and M. M. Telo da Gama, "Phase behavior of a binary mixture of patchy colloids: Effect of particle size and gravity," J. Chem. Phys. **155**, 044903 (2021).

[28]X. Xia, H. Hu, M. P. Ciamarra, and R. Ni, "Linker-mediated self-assembly of mobile DNA-coated colloids," Sci. Adv. **6**, eaaz6921 (2020).

[29]J. Kang, S. A. Valenzuela, E. Y. Lin, M. N. Dominguez, Z. M. Sherman, T. M. Truskett, E. V. Anslyn, and D. J. Milliron, "Colorimetric quantification of linking in thermoreversible nanocrystal gel assemblies," Sci. Adv. **8**, eabm7364 (2022).

[30]M. Gouveia, C. S. Dias, and J. M. Tavares, "Percolation in binary mixtures of linkers and particles: Chaining vs branching," J. Chem. Phys. **157**, 164903 (2022); arXiv:2208.10869.

[31]M. Singh, Z. M. Sherman, D. J. Milliron, and T. M. Truskett, "Linker-templated structure tuning of optical response in plasmonic nanoparticle gels," J. Phys. Chem. C **126**, 16885–16893 (2022).

[32]T. Kwon, T. A. Wilcoxson, D. J. Milliron, and T. M. Truskett, "Dynamics of equilibrium-linked colloidal networks," J. Chem. Phys. **157**, 184902 (2022); arXiv:2209.04580.

[33]A. Nag, D. S. Chung, D. S. Dolzhnikov, N. M. Dimitrijevic, S. Chattopadhyay, T. Shibata, and D. V. Talapin, "Effect of metal ions on photoluminescence, charge transport, magnetic and catalytic properties of all-inorganic colloidal nanocrystals and nanocrystal solids," J. Am. Chem. Soc. **134**, 13604–13615 (2012).

[34]I. D. Stoev, T. Cao, A. Caciagli, J. Yu, C. Ness, R. Liu, R. Ghosh, T. O'Neill, D. Liu, and E. Eiser, "On the role of flexibility in linker-mediated DNA hydrogels," Soft Matter **16**, 990–1001 (2020).

[35]J. Yang, N. J. Kramer, K. S. Schramke, L. M. Wheeler, L. V. Besteiro, C. J. Hogan, Jr., A. O. Govorov, and U. R. Kortshagen, "Broadband absorbing exciton–plasmon metafluids with narrow transparency windows," Nano Lett. **16**, 1472–1477 (2016).

[36]E. V. Shevchenko, D. V. Talapin, N. A. Kotov, S. O'Brien, and C. B. Murray, "Structural diversity in binary nanoparticle superlattices," Nature **439**, 55–59 (2006).

[37]E. V. Shevchenko, D. V. Talapin, C. B. Murray, and S. O'Brien, "Structural characterization of self-assembled multifunctional binary nanoparticle superlattices," J. Am. Chem. Soc. **128**, 3620–3637 (2006).

[38]K. L. Young, M. B. Ross, M. G. Blaber, M. Rycenga, M. R. Jones, C. Zhang, A. J. Senesi, B. Lee, G. C. Schatz, and C. A. Mirkin, "Using DNA to design plasmonic metamaterials with tunable optical properties," Adv. Mater. **26**, 653–659 (2014).

[39]E. V. Shevchenko, M. Ringler, A. Schwemer, D. V. Talapin, T. A. Klar, A. L. Rogach, J. Feldmann, and A. P. Alivisatos, "Self-assembled binary superlattices of CdSe and Au nanocrystals and their fluorescence properties," J. Am. Chem. Soc. **130**, 3274–3275 (2008).

[40]K. Hosoki, T. Tayagaki, S. Yamamoto, K. Matsuda, and Y. Kanemitsu, "Direct and stepwise energy transfer from excitons to plasmons in close-packed metal and semiconductor nanoparticle monolayer films," Phys. Rev. Lett. **100**, 207404 (2008).

[41]M. Cargnello, A. C. Johnston-Peck, B. T. Diroll, E. Wong, B. Datta, D. Damodhar, V. V. T. Doan-Nguyen, A. A. Herzing, C. R. Kagan, and C. B. Murray, "Substitutional doping in nanocrystal superlattices," Nature **524**, 450–453 (2015).

[42]Q. Shi, D. Sikdar, R. Fu, K. J. Si, D. Dong, Y. Liu, M. Premaratne, and W. Cheng, "2D binary plasmonic nanoassemblies with semiconductor n/p-doping-like properties," Adv. Mater. **30**, 1801118 (2018).

[43]V. Lesnyak, A. Wolf, A. Dubavik, L. Borchardt, S. V. Voitekhovich, N. Gaponik, S. Kaskel, and A. Eychmüller, "3D assembly of semiconductor and metal nanocrystals: Hybrid CdTe/Au structures with controlled content," J. Am. Chem. Soc. **133**, 13413–13420 (2011).

[44]A. Wolf, V. Lesnyak, N. Gaponik, and A. Eychmüller, "Quantum-dot-based (aero)gels: Control of the optical properties," J. Phys. Chem. Lett. **3**, 2188–2193 (2012).

[45]T. Hendel, V. Lesnyak, L. Kühn, A.-K. Herrmann, N. C. Bigall, L. Borchardt, S. Kaskel, N. Gaponik, and A. Eychmüller, "Mixed aerogels from Au and CdTe nanoparticles," Adv. Funct. Mater. **23**, 1903–1911 (2013).

[46]A.-K. Herrmann, P. Formanek, L. Borchardt, M. Klose, L. Giebeler, J. Eckert, S. Kaskel, N. Gaponik, and A. Eychmüller, "Multimetallic aerogels by template-free self-assembly of Au, Ag, Pt, and Pd nanoparticles," Chem. Mater. **26**, 1074–1083 (2014).

[47]R. Wendt, B. Märker, A. Dubavik, A.-K. Herrmann, M. Wollgarten, Y. P. Rakovich, A. Eychmüller, K. Rademann, and T. Hendel, "Versatile H_2O_2-driven mixed aerogel synthesis from CdTe and bimetallic noble metal nanoparticles," J. Mater. Chem. C **5**, 10251–10259 (2017).

[48]A. Freytag, C. Günnemann, S. Naskar, S. Hamid, F. Lübkemann, D. Bahnemann, and N. C. Bigall, "Tailoring composition and material distribution in multicomponent cryoaerogels for application in photocatalysis," ACS Appl. Nano Mater. **1**, 6123–6130 (2018).

[49]J. L. Davis, K. L. Silva, and S. L. Brock, "Exploiting kinetics for assembly of multicomponent nanoparticle networks with programmable control of heterogeneity," Chem. Commun. **56**, 458–461 (2020).

[50]M. Rosebrock, D. Zámbó, P. Rusch, D. Pluta, F. Steinbach, P. Bessel, A. Schlosser, A. Feldhoff, K. D. J. Hindricks, P. Behrens, D. Dorfs, and N. C. Bigall, "Spatial extent of fluorescence quenching in mixed semiconductor–metal nanoparticle gel networks," Adv. Funct. Mater. **31**, 2101628 (2021).

[51]P. Rusch, D. Pluta, F. Lübkemann, D. Dorfs, D. Zámbó, and N. C. Bigall, "Temperature and composition dependent optical properties of CdSe/CdS dot/rod-based aerogel networks," ChemPhysChem **23**, e202100755 (2022).

[52]A. Schlosser, J. Schlenkrich, D. Zámbó, M. Rosebrock, R. T. Graf, G. Escobar Cano, and N. C. Bigall, "Interparticle interaction matters: Charge carrier dynamics in hybrid semiconductor–metal cryoaerogels," Adv. Mater. Interfaces **9**, 2200055 (2022).

[53]Z. M. Sherman, K. Kim, J. Kang, B. J. Roman, H. S. N. Crory, D. L. Conrad, S. A. Valenzuela, E. Y. Lin, M. N. Dominguez, S. L. Gibbs, E. V. Anslyn, D. J. Milliron, and T. M. Truskett, "Plasmonic response of complex nanoparticle assemblies," chemRxiv:2022-rkqw8 (2022).

[54]A. W. Jansons and J. E. Hutchison, "Continuous growth of metal oxide nanocrystals: Enhanced control of nanocrystal size and radial dopant distribution," ACS Nano **10**, 6942–6951 (2016).

[55]S. H. Cho, S. Ghosh, Z. J. Berkson, J. A. Hachtel, J. Shi, X. Zhao, L. C. Reimnitz, C. J. Dahlman, Y. Ho, A. Yang, Y. Liu, J.-C. Idrobo, B. F. Chmelka, and D. J. Milliron, "Syntheses of colloidal F:In_2O_3 cubes: Fluorine-induced faceting and infrared plasmonic response," Chem. Mater. **31**, 2661–2676 (2019).

[56]S. H. Cho, K. M. Roccapriore, C. K. Dass, S. Ghosh, J. Choi, J. Noh, L. C. Reimnitz, S. Heo, K. Kim, K. Xie, B. A. Korgel, X. Li, J. R. Hendrickson, J. A. Hachtel, and D. J. Milliron, "Spectrally tunable infrared plasmonic F,Sn:In_2O_3 nanocrystal cubes," J. Chem. Phys. **152**, 014709 (2020).

[57]J. A. Anderson, J. Glaser, and S. C. Glotzer, "HOOMD-blue: A Python package for high-performance molecular dynamics and hard particle Monte Carlo simulations," Comput. Mater. Sci. **173**, 109363 (2020).

[58]H. N. W. Lekkerkerker and R. Tuinier, *Colloids and the Depletion Interaction* (Springer, New York, 2011).

[59]M. G. Noro and D. Frenkel, "Extended corresponding-states behavior for particles with variable range attractions," J. Chem. Phys. **113**, 2941–2944 (2000).

[60]E. Zaccarelli, P. J. Lu, F. Ciulla, D. A. Weitz, and F. Sciortino, "Gelation as arrested phase separation in short-ranged attractive colloid–polymer mixtures," J. Phys.: Condens. Matter **20**, 494242 (2008).

[61]C. K. Ofosu, T. M. Truskett, and D. J. Milliron, "Solvent-ligand interactions govern stabilizing repulsions between colloidal metal oxide nanocrystals," J. Phys. Chem. Lett. **13**, 11323–11329 (2022); chemRxiv:2022-0hx82 (2022).
[62]D. M. Heyes and J. R. Melrose, "Brownian dynamics simulations of model hard-sphere suspensions," J. Non-Newtonian Fluid Mech. **46**, 1–28 (1993).
[63]S. L. Gibbs, C. M. Staller, A. Agrawal, R. W. Johns, C. A. Saez Cabezas, and D. J. Milliron, "Intrinsic optical and electronic properties from quantitative analysis of plasmonic semiconductor nanocrystal ensemble optical extinction," J. Phys. Chem. C **124**, 24351–24360 (2020).
[64]K. Hayashi, F. Okamoto, S. Hoshi, T. Katashima, D. C. Zujur, X. Li, M. Shibayama, E. P. Gilbert, U.-i. Chung, S. Ohba, T. Oshika, and T. Sakai, "Fast-forming hydrogel with ultralow polymeric content as an artificial vitreous body," Nat. Biomed. Eng. **1**, 0044 (2017).
[65]E. Auyeung, T. I. N. G. Li, A. J. Senesi, A. L. Schmucker, B. C. Pals, M. O. de Ia Cruz, and C. A. Mirkin, "DNA-mediated nanoparticle crystallization into Wulff polyhedra," Nature **505**, 73–77 (2014).
[66]R. T. Scarlett, M. T. Ung, J. C. Crocker, and T. Sinno, "A mechanistic view of binary colloidal superlattice formation using DNA-directed interactions," Soft Matter **7**, 1912–1925 (2011).
[67]P. J. Santos, P. A. Gabrys, L. Z. Zornberg, M. S. Lee, and R. J. Macfarlane, "Macroscopic materials assembled from nanoparticle superlattices," Nature **591**, 586–591 (2021).
[68]D. Jishkariani, K. C. Elbert, Y. Wu, J. D. Lee, M. Hermes, D. Wang, A. Van Blaaderen, and C. B. Murray, "Nanocrystal core size and shape substitutional doping and underlying crystalline order in nanocrystal superlattices," ACS Nano **13**, 5712–5719 (2019).
[69]S. L. Gibbs, C. M. Staller, and D. J. Milliron, "Surface depletion layers in plasmonic metal oxide nanocrystals," Acc. Chem. Res. **52**, 2516–2524 (2019).
[70]J. F. Reuther, S. D. Dahlhauser, and E. V. Anslyn, "Tunable orthogonal reversible covalent (TORC) bonds: Dynamic chemical control over molecular assembly," Angew. Chem., Int. Ed. **58**, 74–85 (2019).